
U-NET BASED PREDICTION OF CEREBROSPINAL FLUID DISTRIBUTION AND VENTRICULAR REFLUX GRADING

A PREPRINT

✉ **Melanie Rieff**^{*1}, ✉ **Fabian Holzberger**¹, ✉ **Oksana Lapina**², ✉ **Geir Ringstad**^{2,4,5,6}, ✉ **Lars Magnus Valnes**³, ✉ **Bogna Warsza**², ✉ **Per Kristian Eide**^{3,5,6}, ✉ **Kent André Mardal**^{5,7,8}, and ✉ **Barbara Wohlmuth**¹

¹Department of Mathematics, School of Computation, Information, and Technology, Technical University of Munich, Garching, Germany

²Department of Radiology, Oslo University Hospital Rikshospitalet, Oslo, Norway

³Department of Neurosurgery, Oslo University Hospital Rikshospitalet, Oslo, Norway

⁴Department of Geriatrics and Internal Medicine, Sorlandet Hospital, Arendal, Norway

⁵KG Jebsen Centre for Brain Fluid Research, Institute of Clinical Medicine, Faculty of Medicine, University of Oslo, Oslo, Norway

⁶Institute of Clinical Medicine, Faculty of Medicine, University of Oslo, Oslo, Norway

⁷Department of Mathematics, University of Oslo, Oslo, Norway

⁸Department of Numerical Analysis and Scientific Computing, Simula Research Laboratory, Oslo, Norway

ABSTRACT

Previous work shows evidence that cerebrospinal fluid (CSF) plays a crucial role in brain waste clearance processes, and that altered flow patterns are associated with various diseases of the central nervous system. In this study, we investigate the potential of deep learning to predict the distribution in human brain of a gadolinium-based CSF contrast agent (tracer) administered intrathecal. For this, T1-weighted magnetic resonance imaging (MRI) scans taken at multiple time points before and after intrathecal injection were utilized. We propose a U-net-based supervised learning model to predict pixel-wise signal increases at their peak after 24 hours. Its performance is evaluated based on different tracer distribution stages provided during training, including predictions from baseline scans taken before injection. Our findings indicate that using imaging data from just the first two hours post-injection for training yields tracer flow predictions comparable to those trained with additional later-stage scans. The model was further validated by comparing ventricular reflux gradings provided by neuroradiologists, and inter-rater grading among medical experts and the model showed excellent agreement. Our results demonstrate the potential of deep learning-based methods for CSF flow prediction, suggesting that fewer MRI scans could be sufficient for clinical analysis, which might significantly improve clinical efficiency, patient well-being, and lower healthcare costs.

Keywords brain clearance · cerebrospinal fluid · deep learning · U-net · glymphatic system · MRI tracer

1 Introduction

Cerebrospinal fluid (CSF) and its elementary roles in cushioning the brain and spinal cord, facilitating buoyancy to prevent nerve roots or blood vessels being compressed and transporting nutrients, have been known for a long time. Recent research findings however dramatically expanded our understanding of CSF, particularly its critical function in brain solute clearance and biomarker transportation [Fame and Lehtinen, 2020, Wichmann et al., 2022, Thomas, 2019, Bjerke and Engelborghs, 2018, Bohr et al., 2022]. The role of CSF in clearing proteins has gained considerable attention, given the main characteristic of neurodegenerative diseases to be abnormal protein aggregation, such as amyloid- β or tau in Alzheimer’s disease (AD) and α -synuclein in Parkinson’s disease [Pingle et al., 2023, Nedergaard and Goldman, 2020]. Apart from that, CSF plays a crucial role in the diagnosis, monitoring, and understanding of

*Corresponding author. Now at: ETH Zurich, Department of Computer Science, Zurich, Switzerland. E-Mail: mrieff@student.ethz.ch

autoimmune, infectious or neuropsychiatric disorders as well as hydrocephalus, idiopathic intracranial hypertension, ischemic stroke, and brain cancers, indicating that changes in fluid dynamics can influence tumor progression and treatment outcomes [Jin and Munson, 2023, Honnorat and Plazat, 2018]. Furthermore, recent scientific findings suggest that CSF helps regulate the sleep-wake cycle, with sleep deprivation linked to disturbed flow dynamics [Eide et al., 2021a, Vinje et al., 2023]. Distorted clearance mechanisms may contribute to the pathogenesis and progression of these conditions, thus an enhanced understanding of CSF dynamics is expected to offer valuable insights into the mechanisms by which molecules are exchanged between the blood, brain, and cerebrospinal fluid, and may ultimately open new therapeutic avenues [Eide et al., 2021b]. Among the various imaging techniques employed for brain clearance analysis, intrathecal contrast-enhanced (CE) MRI methods have been well-established in clinical practice [Ringstad et al., 2017]. They permit in vivo tracking of an exogenous tracer to mirror the behavior of endogenous solutes within the brain, but necessitate a series of MRI scans, which results in inpatient admission, and consequently, significant healthcare costs. Previous research on CSF analysis has used various mathematical and computational models to understand its dynamics and relationship with neurological conditions. However, these models often depend on advanced computational resources or medical assumptions made in the modeling process [Valnes et al., 2020, Zapf et al., 2022, Hornkjøl et al., 2022, Zeinhofer and Mardal, 2024]. Given that distribution patterns vary considerably across different neurodegenerative conditions [Ringstad et al., 2017, Eide et al., 2020] and the increasing availability of data, a more robust and flexible approach should be employed. In that context, data driven machine learning, and particularly deep learning could be a promising alternative incorporating hidden behaviors observed only in data. Despite the advancements in both traditional and machine learning techniques, there remains a gap in the direct application of deep learning to forecast CSF flow. In this study, we investigate the use of a convolutional neural network (CNN) in tracer analysis and evaluate how well deep learning-based methods are able to predict CSF tracer distribution patterns. Besides evaluating image similarity of predicted MRI scans compared to real imaging data using evaluation metrics common in deep learning, we additionally use a clinically oriented reflux assessment scheme as a method to judge the model’s performance. This is relevant because assessment of ventricular reflux has been found clinically useful in the diagnostic pre-operative work-up of idiopathic normal pressure hydrocephalus (iNPH) [Eide et al., 2020, 2021b]. The present findings demonstrate the use of deep learning techniques in CSF distribution prediction and indicate that repeated MRI may be avoided, resulting in reduced medical cost, consumed clinical resources, as well as patient burden.

2 Related work

Previous research on cerebrospinal fluid analysis has employed various mathematical and computational modeling approaches to understand its dynamics and interplay with several neurological conditions. CNNs, for example, were utilized numerous times to predict AD from brain MRI data, though almost exclusively not contrast-enhanced. Pathological molecular hallmarks of AD, such as amyloid- β -42 and tau proteins, were quantified using an ensemble-based model [Popuri et al., 2020]. Schweizer et al. examined the potential to use CNNs for classification of individual cells that CSF contains [Schweizer et al., 2023], and real-time CSF flow velocities were estimated using inflow effect-mediated signal increase of in vivo functional MRI [Diorio et al., 2024]. Four-dimensional flow of CSF has been assessed with various patient cohorts, fluid markers, and regions of interest [Rivera-Rivera et al., 2024], although the limitations of this imaging approach due to low velocities associated with CSF motion and large T1 relaxation values were continuously faced. While well-established mathematical approaches such as mesh-based finite element methods and partial differential equation-constrained optimization were used to directly model diffusion of CSF in the human brain [Valnes et al., 2020], they face some drawbacks such as high computational cost and the need of high-quality meshes to simulate complex geometries. Quite recently, physics-informed neural networks (PINNs) were introduced to integrate physical laws into neural networks for various applications, including heat transfer and diffusion. Zapf et al. [Vinje et al., 2023, Zapf et al., 2022] highlighted the potential of PINNs in solving inverse problems governed by partial differential constrained optimization, which were extended to estimate the apparent diffusion coefficient of cerebrospinal fluid tracers in specific regions of interest in the brain (subcortical white matter subregiona and full brain parenchyma) and experimentally validated with MRI data from sleep-deprived patients. Their findings suggest that diffusion alone may not be sufficient to model molecule distribution or clearance in the brain, supporting the glymphatic model’s perspective on molecular transport. In the domain of computational fluid dynamics, physiological boundary conditions improved the simulations of intracranial pressures and flow velocities through the cerebral aqueduct and spinal subarachnoid space (SAS) [Vandenbulcke et al., 2022]. While the aforementioned approaches each offer insights into cerebrospinal fluid modeling, they all rely on specific assumptions and simplifications that may not universally represent the complex process of CSF distribution and clearance across different conditions; thus, in our study, we employ deep learning techniques, which do not require prior information about brain anatomy, CSF production, circulation, or volume properties, aiming to offer a more generalized solution.

Table 1: Patient material

	N	Age	Sex (Female/Male)	Body mass index kg m^{-2}
Total cohort	136	48.0 \pm 18.2	85/51	27.7 \pm 5.1
References	25	35.9 \pm 10.4	21/4	27.9 \pm 5.4
Arachnoid cyst (AC)	17	48.1 \pm 16.9	9/8	26.7 \pm 2.8
Pineal cyst (PC)	14	37.1 \pm 13.0	13/1	28.1 \pm 4.7
Idiopathic intracranial hypertension (IIH)	16	34.6 \pm 11.8	14/2	31.7 \pm 5.1
Spontaneous intracranial hypotension (SIH)	15	48.1 \pm 14.7	11/4	25.7 \pm 6.2
Idiopathic normal pressure hydrocephalus (iNPH)	33	70.8 \pm 6.5	9/24	27.0 \pm 4.2
Hydrocephalus (HC)	16	42.6 \pm 14.5	8/8	27.3 \pm 6.0

3 Materials and Methods

3.1 Study population

This was a single-center retrospective study that utilized MRI data from a cohort of 136 patients of different neurological conditions. Table 1 shows the distribution of neuropathological findings for all of the analyzed data.

3.2 Injection protocol, MRI hardware, and data preprocessing

To evaluate the enrichment of a CSF tracer in the human brain, the MRI contrast agent gadobutrol was utilized as CSF tracer. An interventional neuroradiologist administered an intrathecal injection of gadobutrol at a dosage of 0.5 mmol (0.5 mL of 1.0 mmol mL⁻¹ gadobutrol; Gadovist, Bayer Pharma AG, Germany). T1-weighted MRI scans were performed before and at various intervals post-injection. For practical reasons, MRI examinations could not be conducted at the exact same times for each study participant, but there is consistency grouping the scans into the following time intervals: 0 hours (before injection, baseline), 1-2 hours, 3-5 hours, 5-6 hours, 6-10 hours, 24 hours, 48 hours, and 29 days (full clearance, control scan). Some patients were scanned multiple times during an interval. We used a 3 Tesla Philips Ingenia MRI scanner (Philips Medical Systems) with equal imaging protocol settings at all time points to acquire sagittal 3D T1-weighted scans. The imaging parameters were: repetition time = ‘shortest’ (typically 5.1 ms), echo time = ‘shortest’ (typically 2.3 ms), flip angle=8 degrees, 256cm \times 256cm field of view and matrix = 256 \times 256 pixels (reconstructed 512 \times 512). The slices were sampled 184 overcontiguous (overlapping) with 1 mm thickness that were automatically reconstructed to 368 slices with 0.5 mm thickness; total duration of each image acquisition was 6 min and 29 s. To secure consistency and reproducibility of the MRI slice placement and orientation, slice orientation of image stacks was defined using an automated anatomy recognition protocol based on landmark detection in MRI data (SmartExamTM, Philips Medical Systems) for every time point. The images for each patient was registered/aligned using FreeSurfer software (version 6.0) (<http://surfer.nmr.mgh.harvard.edu/>) and re-sampled to the FreeSurfer standard of 256³ voxels with voxel size of 1.0mm \times 1.0mm \times 1.0mm [Eide et al., 2021a,b, Ringstad et al., 2018]. The images was normalized by dividing the signal values with the mean signal value of a reference volume within the intraconal orbital fat [Eide et al., 2021a]. Then, each images were centered and the sagittal and axial slices were exported as 256 \times 256 matrices. For predicting tracer distribution after 24 hours, we fed our model with different information during training and compared the results. For grayscale images, possible intensities range from 0 (black) to 1 (white) and in between different shades of gray, as shown in Figure 1 for illustrative purposes.

3.3 Distribution and clearance pattern

A series of T1-weighted images of the patient taken after intrathecal tracer administration, exemplified in Fig. 2, shows the tracer transport and elimination mechanisms. Following the injection of gadobutrol into the spinal canal at the lumbar region, the tracer ascends through the spinal canal, and typically reaches the subarachnoid space (SAS) at the level of the foramen magnum [Liu et al., 2022, Dreha-Kulaczewski et al., 2015]. Significant spinal resorption means that only about 25 % of the injected tracer reaches intracranial space [Vinje et al., 2023, Eide et al., 2021c]. Once in the cisterna magna, the tracer rapidly moves to subarachnoid cisterns and then distributes along major arteries within the cerebral fissures. To evaluate the enrichment of a CSF tracer in the human brain, the MRI contrast agent gadobutrol was utilized as CSF tracer, showing significant accumulation in areas adjacent to the major arteries [Vinje et al., 2023, Ringstad et al., 2018]. MRI scans performed 24 hours after injection reveal diffuse tracer enhancement around the brain, with signal enhancement peaking typically at 24 hours after injection [Ringstad et al., 2017]. Gadobutrol clearance

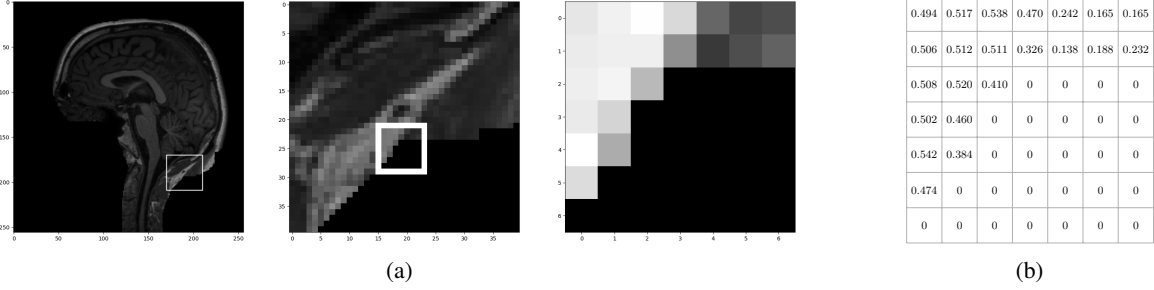


Figure 1: Conversion of grayscale MRI scans of size 256×256 to a matrix of this size. 1a Cropping a sample image to a subregion of size 7×7 pixels for illustration. 1b Each pixel is assigned a number from 0 (all black) to 1 (all white) and in between shades of gray.

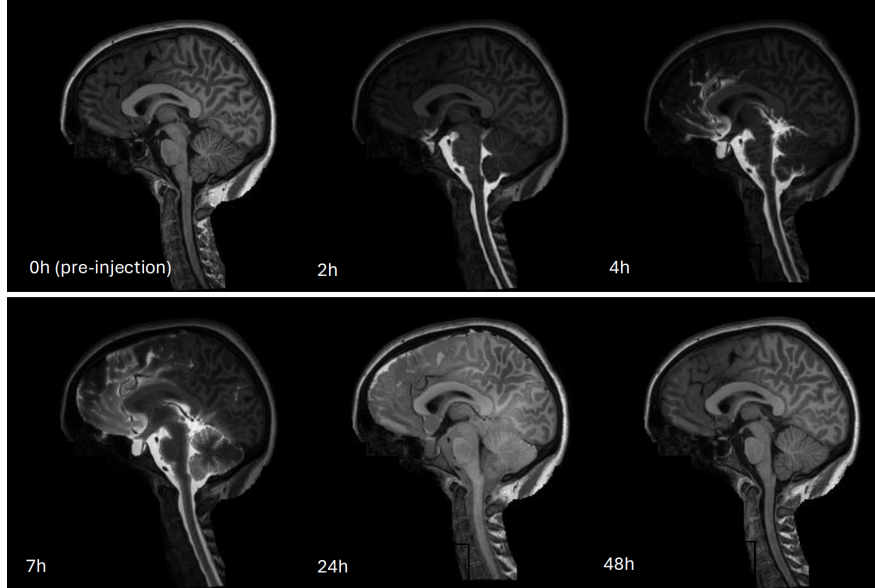


Figure 2: Defaced sagittal slices from CSF tracer-enhanced MRI of a sample patient. After 24 hours, the tracer has enriched the CSF spaces around the entire brain and is completely cleared after four weeks.

is driven by resorption initially from the spinal canal, and peak gadobutrol concentration in the blood occurs around five to six hours after injection [Eide et al., 2021c, Hovd et al., 2022, Shah et al., 2023, Melin et al., 2023]. At the four-week post-injection mark, MRI scans reveal no evidence of contrast agent accumulation in the brain. Still, the exact underlying mechanisms of tracer distribution and clearance remain not fully understood [Plog and Nedergaard, 2018, Iliff et al., 2012].

3.4 Model architecture

Inference in neural networks can be described by the equation $\hat{y} = f(x; W)$, where x is the input, W are weights of the network, and \hat{y} is the output, i.e., the prediction. Training a neural network corresponds to finding the solution \hat{W} of the loss minimization problem

$$\hat{W} = \arg \min_W L(W, \mathcal{D}) = \arg \min_W \frac{1}{N} \sum_{i=1}^N \ell(f_W(x_i), y_i),$$

where ℓ is a given loss function and $\mathcal{D} = \{(x_1, y_1), (x_2, y_2), \dots, (x_N, y_N)\}$ is the training data. There exists a variety of loss functions. Here, we use a regression model and compare the two commonly chosen loss functions: the ℓ_2 -loss defined as $\ell_2(\hat{y}, y) = (\hat{y} - y)^2$, and the ℓ_1 -loss, defined as $\ell_1(\hat{y}, y) = |\hat{y} - y|$. Experimenting with different loss functions is a crucial part of designing a deep learning model, because the choice of the loss function significantly

impacts the model’s performance, behavior, and convergence during training, which has been shown a number of times [Shan et al., 2023]. Figure 3 depicts a simplified illustration of the training process.

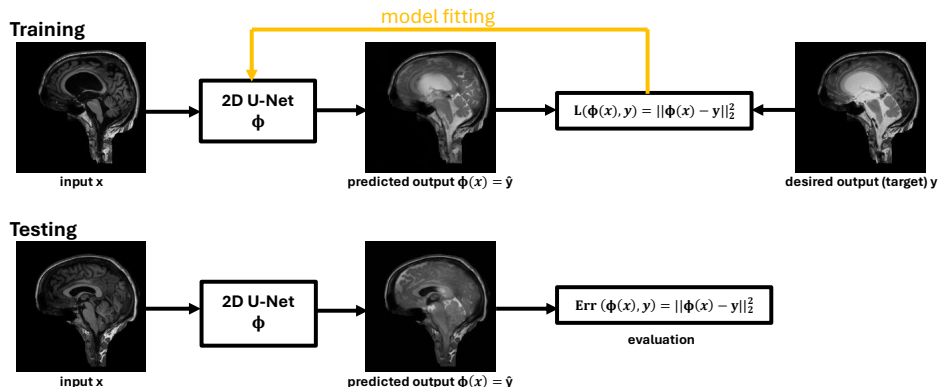
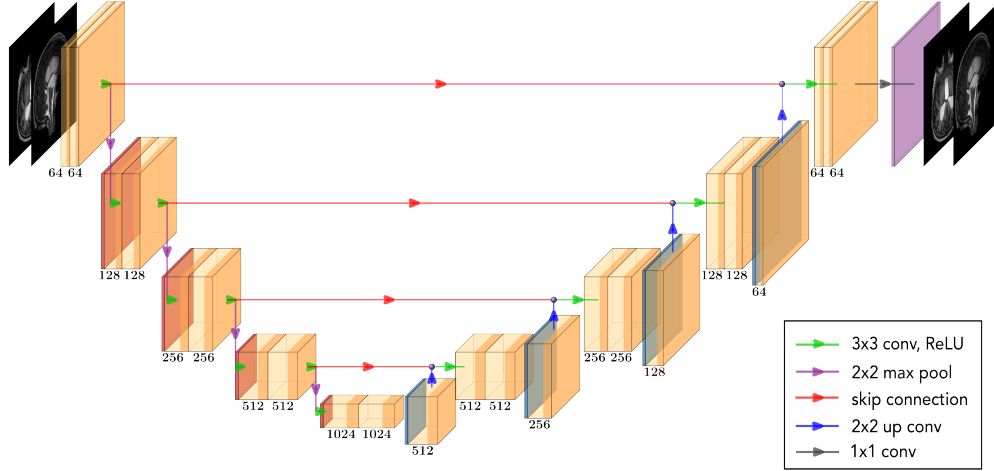


Figure 3: Exemplary illustration of the training and testing steps. Here, the network was trained by minimizing the ℓ_2 -loss of the reconstructed sagittal images to the real images and final model evaluation made use of the mean of all squared errors among the testing data.

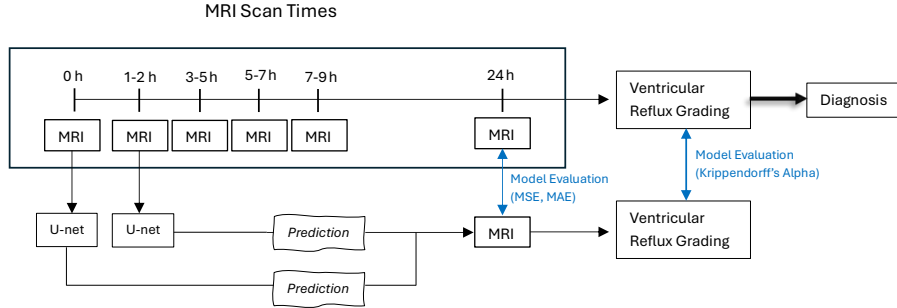
In this study, we used a U-net architecture for the prediction of the tracer distribution. Introduced by Olaf Ronneberger et al. in 2015 [Ronneberger et al., 2015], U-net is a model originally proposed for 2D or 3D image segmentation, particularly in biomedical applications [Cai and Yuan, 2022, Siddique et al., 2021]. Thereafter, it served as a blueprint for a plethora of variations that have so far been proposed and used in several application areas [Wang et al., 2023, Azad et al., 2022, Pai and M., 2023], which all share a common structure inspired by an encoder-decoder architecture comprising two primary paths: the contracting (or compressive) path and the expansive (or up-sampling) path. The contracting path functions similarly to a convolutional neural network (CNN), where images are down-sampled at first using a convolutional kernel followed by an activation function. Conversely, the expansive path up-samples the compressed representation to reconstruct the image. In addition, skip connections link the corresponding layers of the contracting and expansive paths, helping to preserve spatial information that is typically lost during the down-sampling process [Wilm et al., 2024]. In contrast to other supervised deep learning methods such as CNNs and fully convolutional neural networks (FCNs), U-nets have a more complicated architecture, yet have been shown to perform better, particularly on medical imaging data and small data sets [Wang et al., 2023, Azad et al., 2022]. Furthermore, U-Net-based models are well-equipped to handle small structures and objects within an image, a capability crucial for accurately predicting tracer fluid distribution. For the implementation of our 2D U-Net architecture, we used PyTorch, a variable number of input channels, 64 features, 8 batch size, Adam optimizer, 200 or 250 epochs, 1×10^{-3} learning rate, 3×3 convolutional kernels followed by batch normalization and rectified linear unit as activation function, and 2×2 maximal pooling size. Batch normalization mitigates the internal covariate shift by normalizing layer inputs, stabilizing and accelerating the training process. It allows higher learning rates, improves the gradient flow, and has a regularizing effect. ReLU, defined as

$$f(x) = \max(0, x),$$

introduces a non-linearity into the network, which is crucial for modeling complex, non-linear relationships. ReLU offers a computationally efficient non-linear transformation, and enhances the network’s efficiency by activating only a subset of neurons, which can lead to a reduced computational load and mitigate the risk of overfitting. Overfitting occurs when a model becomes too tailored to the training data, capturing noise and specific patterns to the extent that it negatively impacts its performance on new, unseen data. Additionally, ReLU helps alleviate the vanishing gradient problem, particularly in deeper networks, by ensuring that gradients remain significant, thereby facilitating more robust and efficient training. Firstly, we use a U-net as illustrated in Figure 4a with two input channels (for sagittal and axial scans, respectively) to use scans from baseline (before injection) as training input. With this, we address how well our model may accurately predict tracer distribution after 24 hours providing it with specific patient anatomy only. Changing the number of input channels allows the model to further use tracer-enriched scans. By comparing the model performance of varying training data, we aim to assess to what extent different tracer distribution stages contribute to better prediction performance. In any model training, the available data is split into 80 % cases for training and the remaining 20 % for testing. Figure 4b provides an overview of the data processing workflow, deep-learning model usage, and clinical interpretation.



(a)



(b)

Figure 4: 4a: Modified U-net architecture used in this work. Here, axial and sagittal MRI planes (one each) scanned before tracer injection are used to predict its distribution 24 hours after tracer injection. 4b: Processing workflow from original MRI scans to U-Net model predictions, comparison with real MRI images, and final clinical diagnosis.

3.5 Ventricular reflux grading

Traditionally, CSF diagnostics with MRI have primarily focused on anatomical abnormalities in the brain [Ahmad et al., 2021]. To analyze cerebrospinal fluid dynamics, a grading scheme was introduced and since then used in clinical assessment of patients [Eide et al., 2020, 2021b]: Ventricular reflux refers to the retrograde movement of CSF from the SAS back into the cerebral ventricles and is measured on an integer scale from 0 to 4. Visually assessed reflux can be categorized into five grades based on the intensity and duration of tracer enrichment within the ventricles, which serves as a critical parameter in evaluating fluid dynamics and can be linked to the efficiency of CSF clearance [Eide et al., 2021b]:

- Grade 0: No supra-aqueductal reflux.
- Grade 1: Sign of supra-aqueductal reflux.
- Grade 2: Transient enrichment of lateral ventricles.
- Grade 3: Lasting enrichment of lateral ventricles at 24 hours, not isointense with CSF subarachnoid.
- Grade 4: Lasting enrichment of lateral ventricles at 24 hours, isointense with CSF subarachnoid.

Reflux grades 3 and 4 have been shown associated with raised intracranial pressure pulsatility, a feature of shunt-responsive iNPH [Eide et al., 2021b, 2020]. Comparing MRI biomarkers of CSF tracer dynamics (including ventricular reflux grades) with anatomical MRI biomarkers of CSF space, markers of neurodegeneration and pulsatile intracranial pressure score showed reduced tracer clearance and higher grades of ventricular reflux (grades 3–4 in shunt-responsive

Table 2: Model errors (test data) to predict gadobutrol distribution 24 hours post-injection based on different scan intervals used as training input.

Evaluation metrics	pre-injection	1-2 hours	3-5 hours	5-7 hours	7-9 hours	1-9 hours
Mean Squared Error	7×10^{-3}	2×10^{-3}	6×10^{-3}	5×10^{-3}	4×10^{-3}	1×10^{-3}
Mean Absolute Error	3.8×10^{-2}	1.8×10^{-2}	3.5×10^{-2}	3.5×10^{-2}	3×10^{-2}	1.3×10^{-2}

idiopathic normal pressure hydrocephalus) [Eide et al., 2020]. In this work, we use the ventricular reflux grading scheme as an additional method of model performance evaluation.

4 Experimental Results

4.1 Image prediction from baseline and tracer-enriched scans

Mean squared error (MSE) $\frac{1}{N} \sum_{i=1}^N (\hat{y}_i - y_i)^2$ and mean absolute error (MAE) $\frac{1}{N} \sum_{i=1}^N |\hat{y}_i - y_i|$ of predicted \hat{y}_i and real scans y_i , each of dimension $256 \times 256 \times 2$ (axial and sagittal plane), were computed using PyTorch. We trained for 250 epochs and achieved 7×10^{-3} MSE and 3.8×10^{-2} MAE for the testing set and 1×10^{-3} MSE and 1×10^{-2} MAE for the training set, indicating overfitting of the model after 50 to 100 epochs. Visual inspection of predictions showed preservation of anatomical characteristics despite some blurriness. Given that the model utilized 129 training scan pairs compared to several thousands in other frameworks (MNIST database: 60,000 training images and 10,000 test images), this reflects outstanding performance and highlights the promising potential of deep learning-based models, particularly in the medical domain, where routinely performed data collection, curation and storage is still rare. A sample test case is depicted in Figure 5.

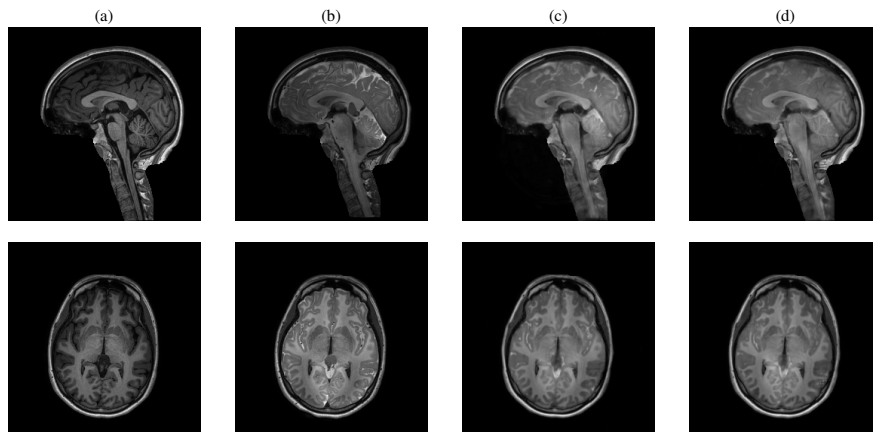


Figure 5: A sample test case (sagittal and axial plane) of gadobutrol distribution prediction based from baseline MRI scans (pre-injection). 5a: real MR imaging taken before injection. 5b: real MR imaging taken approximately 24 hours after intrathecal tracer injection. 5c: predicted tracer distribution 24 hours post-injection using an ℓ_2 loss function. 5d: predicted tracer distribution using an ℓ_1 loss function.

Table 2 summarizes achieved errors on the test data set for different MR imaging time intervals used as training data. Mean squared errors resulted in the order of magnitude 1×10^{-3} , while mean absolute errors were in the order of magnitude 1×10^{-2} . Remarkably, training solely on data obtained 1-2 hours post-injection showed slightly better performance (MSE 2×10^{-3}) compared to tracer-enriched MR scans obtained 3-5 hours, 5-7 hours, or 7-9 hours after intrathecal gadobutrol injection (MSEs 6×10^{-3} , 5×10^{-3} , 4×10^{-3} , respectively). We experimentally found that using the ℓ_2 -loss generally predicts anatomical structures with more precision compared to an ℓ_1 loss function. Two randomly drawn test cases showing real and predicted MR imaging are displayed in Figure 6. Train and test losses during the U-net training process (ℓ_2 -loss) are displayed in Appendix 7.

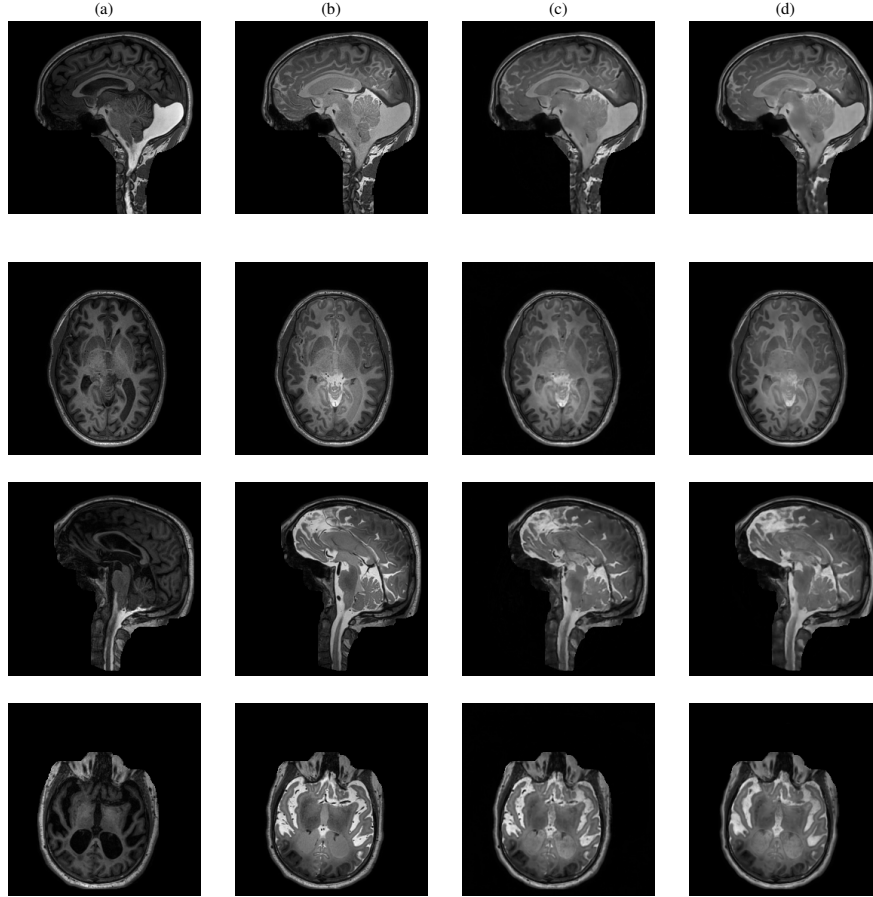


Figure 6: Two sample test cases (sagittal and axial plane) of gadobutrol distribution prediction based from MRI scans obtained 1-2 hours post-injection. 6a: real MR imaging taken within 1-2 hours post-injection. 6b: real MR imaging taken approximately 24 hours after intrathecal tracer injection. 6c: predicted tracer distribution 24 hours post-injection (ℓ_2 loss). 6d: predicted tracer distribution 24 hours post-injection (ℓ_1 loss).

4.2 Ventricular reflux grading performance compared with neuroradiologist assessments

The U-net model trained on scans displaying the tracer distribution within the first two hours after tracer injection was further evaluated with the ventricular reflux grading scheme, which has been used in clinical CSF patient assessment. For this purpose, three human raters (board-certified neuroradiologists) were asked to assign the ventricular reflux grading on 62 sagittal-axial scan pairs that display tracer distribution after 24 hours; half of which were original scans taken at this time (ground truth, GT), while the other half were corresponding predicted images generated by our model. Raters were blinded both for clinical information and whether an image was real or artificial. To avoid bias by memorizing patient-specific characteristics, rating was done in two installments such that at no time human raters had the chance to compare real and artificial scans of the same individual. Furthermore, this procedure was done for both loss functions to assess different model architecture performance. The mean model prediction accuracy over all three raters was 89.2% for ℓ_1 - and ℓ_2 -loss. Because of a natural inter-rater variability in ventricular reflux grading [Eide et al., 2020], we further used Krippendorff’s alpha with interval metric to evaluate the model performance. This statistical measure is designed to assess the reliability of coding in content analysis, particularly when multiple observers are involved, and offers high flexibility in handling different types of data, including nominal, ordinal, interval, and ratio scales. Krippendorff’s alpha is defined as the proportion of observed agreement to the agreement expected by chance, adjusted for the level of disagreement among raters. Its mathematical definition is given by $\alpha = 1 - D_O/D_E$, where D_O denotes the observed disagreement, and D_E represents the expected disagreement under the assumption of random coding. This formula ensures that the measure accounts not only for simple agreement but also adjusts for chance agreement, which is crucial in providing an accurate estimate of reliability. Its range extends from negative values, indicating systematic disagreements, to 1, reflecting perfect agreement among coders. An alpha value of 0 denotes agreement equivalent to that expected by chance. In practice, values above 0.8 are typically considered indicative of

Table 3: Krippendorff’s alpha values of agreement between grading of three neuroradiologists on ground truth (GT) and predicted scans. Based on the evaluation of 62 image pairs (31 GT, 31 predicted, two planes each) inter-rater reliability between three human raters on GT (0.856 for ℓ_2 -loss) was inferior compared with the agreement of three human raters each and the model (mean 0.920, range 0.884 - 0.936 for ℓ_2 -loss).

	U-Net (ℓ_2 -loss)	U-Net (ℓ_1 -loss)
Rater 1 on GT and predictions	0.940	0.871
Rater 2 on GT and predictions	0.936	0.822
Rater 3 on GT and predictions	0.884	0.869
All raters on GT	0.856	0.869
All raters on predictions	0.878	0.873

high reliability, although the threshold for acceptability can vary depending on the context of the study and the nature of the data being analyzed. In this analysis, agreement of three human raters each and the model (mean 0.920, range 0.884 - 0.936 for ℓ_2 -loss) evaluated equal or superior compared with inter-rater reliability between three human raters on GT (0.856 for ℓ_2 -loss). A full analysis of Krippendorff’s alpha values is shown in table 3.

5 Discussion

The main observation of this study was that U-net based deep learning provided a high pixel-wise accuracy in predicting the 24-hour distribution imaging utilizing images obtained within 1-2 hours post-injection. These results suggest that the current clinical practice of extended MR imaging sessions to capture later stages of tracer distribution could be reduced without sacrificing diagnostic accuracy. This may provide for improved cost-efficiency and patient throughput.

Traditionally, phase-contrast magnetic resonance imaging (PC-MRI) has been used to assess CSF flow in vivo [Eide et al., 2021b]; however, this method has limitations, and tracer studies using contrast agents as CSF tracers may have advantages. A disadvantage with tracer studies is the need for several MRI acquisitions, which not only place significant burden on patients, but are also resource-intensive. The present results document that deep learning-based approaches may be used to avoid repetitive MRI acquisitions.

The machine learning approach may even be better than the human assessment. In addition to error metrics common in neural network regression, we evaluated the model performance by comparing the grading of ventricular reflux on both real scans and those predicted by our model. Inter-rater reliability between the human raters and the model was generally higher than the reliability between human raters alone, indicating that the artificially generated MR scans of the human brain could be equally conclusive for diagnostic CSF assessment.

Some limitation should be noted. While the proposed U-net-based deep learning model demonstrates potential in predicting CSF tracer distribution and assessing ventricular reflux, two limitations of this study should be noted. First, our study is based on a small cohort size of 136 patients with different underlying diseases, which may limit the generalizability of the model’s performance across diverse populations. Second, we utilize a 2D U-net architecture for image prediction, which limits its effectiveness in capturing the full complexity of 3D anatomical structures. Utilization of 3D volumetric data is desirable in the clinical setting, as neuroradiologists commonly assess CSF dynamics and ventricular reflux grading scores across multiple planes.

Future prospects are the use of sufficient computational resources that will give further research opportunities, ideally leveraging volumetric 3D data and integrating this data into a 3D U-net architecture. Another promising direction for future research lies in predicting specifically the tracer clearance process, particularly after the peak distribution at roughly 24 hours post-injection. It remains an open question whether data from the first one to ten hours post-injection are satisfactory to predict decline of tracer signal with a similar deep-learning approach, which would provide further insights into potentially disturbed flow patterns. Understanding the clearance process is crucial, as delayed clearance serves as pathophysiological indicator of several conditions related to neurodegenerative decline, such as in idiopathic normal pressure hydrocephalus (iNPH), Alzheimer’s, and Parkinson’s disease [Hornkjøl et al., 2022, Lopes et al., 2022]. Furthermore, integrating clinical measurements, outcomes and longitudinal data, such as patient demographic information, neurocognitive assessment scores, blood work, CSF biomarkers, and patient-specific tracer concentration could enhance the prediction performance and offer more comprehensive evaluations of the model’s predictive capabilities and clinical utility.

In summary, U-net based deep learning was found useful for predicting tracer distribution 24 hours after its intrathecal administration. This may have clinical implications by reducing the number of MRI acquisitions, but further research is required to implement such a methodology in 3D MRI that is used clinically.

Author contributions

MR conducted the experiments, performed analysis, and drafted the manuscript under supervision of FH, BW, KAM, and PKE. LMV prepared the experimental data. GR, BW, and OL provided grading of medical images. All authors have read the manuscript, provided critical feedback and approved the final version.

References

- Ryan M. Fame and Maria K. Lehtinen. Emergence and developmental roles of the cerebrospinal fluid system. *Developmental Cell*, 52(3):261–275, 2020. doi:10.1016/j.devcel.2020.01.027.
- Thea Overgaard Wichmann, Helle Hasager Damkier, and Michael Pedersen. A brief overview of the cerebrospinal fluid system and its implications for brain and spinal cord diseases. *Front Hum Neurosci*, 15, 2022. doi:10.3389/fnhum.2021.737217.
- John H. Thomas. Fluid dynamics of cerebrospinal fluid flow in perivascular spaces. *J R Soc Interface*, 16(159), 2019. doi:10.1098/rsif.2019.0572.
- Maria Bjerke and Sebastian Engelborghs. Cerebrospinal fluid biomarkers for early and differential alzheimer’s disease diagnosis. *Perry G, Avila J, Tabaton M, Zhu X, eds. JAD*, 62(3):1199–1209, 2018. doi:10.3233/JAD-170680.
- Tomas Bohr, Poul G. Hjorth, Sebastian C. Holst, et al. The glymphatic system: Current understanding and modeling. *iScience*, 25(9), 2022. doi:10.1016/j.isci.2022.104987.
- Sandeep C. Pingle, Feng Lin, Misa S. Anekoji, C. Pawan K. Patro, Souvik Datta, Lawrence D. Jones, Santosh Kesari, and Shashaanka Ashili. Exploring the role of cerebrospinal fluid as analyte in neurologic disorders. *Future Sci OA*, 9(4), 2023. doi:10.2144/foa-2023-0006.
- Maiken Nedergaard and Steven A. Goldman. Glymphatic failure as a final common pathway to dementia. *Science*, 370(6512):50–56, 2020. doi:10.1126/science.abb8739.
- Peng Jin and Jennifer M. Munson. Fluids and flows in brain cancer and neurological disorders. *WIREs Mech Dis.*, 15(1), 2023. doi:10.1002/wsbm.1582.
- J. Honnorat and L. O. Plazat. Autoimmune encephalitis and psychiatric disorders. *Revue Neurologique*, 174(4):228–236, 2018. doi:10.1016/j.neurol.2017.11.004.
- Per Kristian Eide, Vegard Vinje, Are Hugo Pripp, Kent-A. Mardal, and Geir Ringstad. Sleep deprivation impairs molecular clearance from the brain. *Brain*, 144(3):863–874, 2021a. doi:10.1093/brain/awaa443.
- Vegard Vinje, Bastian Zapf, Geir Ringstad, Per Kristian Eide, Marie E. Rognes, and Kent-A. Mardal. Human brain solute transport quantified by glymphatic MRI-informed biophysics during sleep and sleep deprivation. *Fluids Barriers CNS*, 20(62), 2023. doi:10.1186/s12987-023-00459-8.
- Per Kristian Eide, Lars Magnus Valnes, E. K. Lindstrøm, Kent-A. Mardal, and Geir Ringstad. Direction and magnitude of cerebrospinal fluid flow vary substantially across central nervous system diseases. *Fluids Barriers CNS*, 18(16), 2021b. doi:10.1186/s12987-021-00251-6.
- Geir Ringstad, Svein-Are S. Vatnehol, and Per Kristian Eide. Glymphatic mri in idiopathic normal pressure hydrocephalus. *Brain*, 140(10):2691–2705, 2017. doi:10.1093/brain/awx191.
- Lars Magnus Valnes, Sebastian K Mitusch, Geir Ringstad, et al. Apparent diffusion coefficient estimates based on 24 hours tracer movement support glymphatic transport in human cerebral cortex. *Sci Rep*, 10(9176), 2020. doi:10.1038/s41598-020-66042-5.
- Bastian Zapf, J Haubner, Miroslav Kuchta, and Geir Ringstad. Investigating molecular transport in the human brain from mri with physics-informed neural networks. *Sci Rep*, 12(15475), 2022. doi:10.1038/s41598-022-19157-w.
- Martin Hornkjøl, Lars Magnus Valnes, Geir Ringstad, et al. Csf circulation and dispersion yield rapid clearance from intracranial compartments. *Front Bioeng Biotechnol*, 2022. doi:10.3389/fbioe.2022.932469.
- Marius Zeinhofer and Kent-Andre Mardal. Signal increase ratio prediction with cnns. In Jørgen Dokken, Kent-Andre Mardal, Marie Rognes, Lars Magnus Valnes, and Vegard Vinje, editors, *Mathematical modeling of the human brain II: from glymphatics to deep learning*. Springer, 2024.

-
- Per Kristian Eide, Are H. Pripp, and Geir Ringstad. Magnetic resonance imaging biomarkers of cerebrospinal fluid tracer dynamics in idiopathic normal pressure hydrocephalus. *Brain Commun.*, 2(2), 2020. doi:10.1093/braincomms/fcaa187.
- Karteek Popuri, Da Ma, Lei Wang, and Mirza Faisal Beg. Using machine learning to quantify structural MRI neurodegeneration patterns of Alzheimer’s disease into dementia score: Independent validation on 8,834 images from ADNI, AIBL, OASIS, and MIRIAD databases. *Hum Brain Mapp*, 31(14):4127–4147, 2020. doi:10.1002/hbm.25115.
- Leonille Schweizer, Philipp Seegerer, Hee-young Kim, Rene Saitenmacher, Amos Muench, et al. Analysing cerebrospinal fluid with explainable deep learning: From diagnostics to insights. *Neuropathol Appl Neurobiol*, 49(1), 2023. doi:10.1111/nan.12866.
- Tyler C. Diorio, Vidha V. Nair, Neal M. Patel, Lauren E. Hedges, Vitaliy L. Rayz, and Yunjie Tong. Real-time quantification of in vivo cerebrospinal fluid velocity using the functional magnetic resonance imaging inflow effect. *NMR in Biomedicine*, 37(10), 2024. doi:10.1002/nbm.5200.
- Leonardo A. Rivera-Rivera, Tomas Vikner, Laura Eisenmenger, Sterling C. Johnson, and Kevin M. Johnson. Four-dimensional flow mri for quantitative assessment of cerebrospinal fluid dynamics: Status and opportunities. *NMR in Biomedicine*, 37(7), 2024. doi:10.1002/nbm.5082.
- Sarah Vandenbulcke, Tim De Pauw, Frank Dewaele, Joris Degroote, and Patrick Segers. Computational fluid dynamics model to predict the dynamical behavior of the cerebrospinal fluid through implementation of physiological boundary conditions. *Front Bioeng Biotechnol*, 10, 2022. doi:10.3389/fbioe.2022.1040517.
- Geir Ringstad, Lars Magnus Valnes, Anders M. Dale, Are H. Pripp, Svein-Are S. Vatnehol, Kyrre E. Emblem, Kent-Andre Mardal, and Per Kristian Eide. Brain-wide glymphatic enhancement and clearance in humans assessed with mri. *JCI Insight*, 3(13), 2018. doi:10.1172/jci.insight.121537.
- Shinuo Liu, Lynne E. Bilston, Neftali Flores Rodriguez, Courtney Wright, Simon McMullan, Robert Lloyd, Marcus A. Stoodley, and Sarah J. Hemley. Changes in intrathoracic pressure, not arterial pulsations, exert the greatest effect on tracer influx in the spinal cord. *Fluids Barriers CNS*, 19(1), 2022. doi:10.1186/s12987-022-00310-6.
- Steffi Dreha-Kulaczewski, Arun A. Joseph, Klaus-Dietmar Merboldt, Hans-Christoph Ludwig, Jutta Gärtner, and Jens Frahm. Inspiration is the major regulator of human csf flow. *J Neurosci*, 35(6):2485–2491, 2015. doi:10.1523/JNEUROSCI.3246-14.2015.
- Per Kristian Eide, Espen Mariussen, Hilde Uggerud, Are H. Pripp, Aslan Lashkarivand, Bjornar Hassel, Hege Christensen, Markus Herberg Hovd, and Geir Ringstad. Clinical application of intrathecal gadobutrol for assessment of cerebrospinal fluid tracer clearance to blood. *JCI Insight*, 6(9), 2021c. doi:10.1172/jci.insight.147063.
- Markus Herberg Hovd, Espen Mariussen, Hilde Uggerud, Aslan Lashkarivand, Hege Christensen, Geir Ringstad, and Per Kristian Eide. Population pharmacokinetic modeling of csf to blood clearance: prospective tracer study of 161 patients under work-up for csf disorders. *Fluids Barriers CNS*, 19(1), 2022. doi:10.1186/s12987-022-00352-w.
- Trishna Shah, Sue E. Leurgans, Rashi I. Mehta, Jingyun Yang, and Chad A. Galloway. Arachnoid granulations are lymphatic conduits that communicate with bone marrow and dura-arachnoid stroma. *J Exp Med*, 220(2), 2023. doi:10.1084/jem.20220618.
- Erik Melin, Geir Ringstad, Lars Magnus Valnes, and Per Kristian Eide. Human parasagittal dura is a potential neuroimmune interface. *Commun Biol*, 6(1), 2023. doi:10.1038/s42003-023-04634-3.
- Benjamin A. Plog and Maiken Nedergaard. The glymphatic system in central nervous system health and disease: Past, present, and future. *Annu Rev Pathol*, 13:379–394, 2018. doi:10.1146/annurev-pathol-051217-111018.
- Jeffrey J. Iliff, Minghuan Wang, Yonghong Liao, et al. A paravascular pathway facilitates csf flow through the brain parenchyma and the clearance of interstitial solutes, including amyloid β . *Sci Transl Med*, 4(147), 2012. doi:10.1126/scitranslmed.3003748.
- Hongming Shan, Rodrigo B. Vimieiro, Lucas R. Borges, Marcelo A.C. Vieira, and Ge Wang. Impact of loss functions on the performance of a deep neural network designed to restore low-dose digital mammography. *Artificial Intelligence in Medicine*, 142:102555, 2023. ISSN 0933-3657. doi:https://doi.org/10.1016/j.artmed.2023.102555.
- Olaf Ronneberger, Philipp Fischer, and Thomas Brox. U-net: Convolutional networks for biomedical image segmentation. In: *Navab, N., Hornegger, J., Wells, W., Frangi, A. (eds) Medical Image Computing and Computer-Assisted Intervention – MICCAI 2015. Lecture Notes in Computer Science, vol 9351. Springer, Cham*, 2015.
- Yi Cai and Jiangying Yuan. A review of u-net network medical image segmentation applications. *Proceedings of the 2022 5th International Conference on Artificial Intelligence and Pattern Recognition.*, 2022. doi:10.1145/3573942.3574048.

-
- Nahian Siddique, Sidike Paheding, Colin P. Elkin, and Vijay Devabhaktuni. U-net and its variants for medical image segmentation: A review of theory and applications. *IEEE Access*, 9:82031–82057, 2021. doi:10.1109/ACCESS.2021.3086020.
- Jundi Wang, Lei Han, and Dongsheng Ran. Architectures and applications of u-net in medical image segmentation: A review. *9th International Symposium on System Security, Safety, and Reliability (ISSSR)*, 2023. doi:10.1109/issr58837.2023.00022.
- Reza Azad, Ehsan Khodapanah Aghdam, Amelie Rauland, Yiwei Jia, Atlas Haddadi Avval, Afshin Bozorgpour, Sanaz Karimijafarbigloo, Joseph Paul Cohen, Ehsan Adeli, and Dorit Merhof. Medical image segmentation review: The success of u-net. <https://arxiv.org/abs/2211.14830>, 2022.
- Ganesh Pai and Sharmila Kumari M. Semi-dense u-net: A novel u-net architecture for face detection. *International Journal of Advanced Computer Science and Applications*, 14(6), 2023. doi:10.14569/IJACSA.2023.0140643. URL <http://dx.doi.org/10.14569/IJACSA.2023.0140643>.
- Frauke Wilm, Jonas Ammeling, Mathias Öttl, Rutger H. J. Fick, Marc Aubreville, and Katharina Breininger. Rethinking u-net skip connections for biomedical image segmentation. <https://arxiv.org/abs/2402.08276>, 2024.
- Nermin Ahmad, Dina Salama, and Mohammad Al-Haggag. Mri csf flowmetry in evaluation of different neurological diseases. *Egypt J Radiol Nucl Medd*, 52(53), 2021. doi:10.1186/s43055-021-00429-w.
- Douglas M. Lopes, Sophie K. Llewellyn, and Ian F. Harrison. Propagation of tau and α -synuclein in the brain: therapeutic potential of the glymphatic system. *Transl Neurodegener*, 11(19), 2022. doi:10.1186/s40035-022-00293-2.

A Appendix

A.1 Loss curves for U-net training and testing over 250 epochs (ℓ_2 loss)

In the loss curve on Figures 7a, 7c, 7d and 7e, we can see that the curve of loss tends to flatten as the epochs number increases, indicating that the training model converges. In 7b and 7f, the gap between training and testing error is smaller, indicating less overfitting and better model performance, which is in accordance to the evaluation metrics shown in Figure 2.

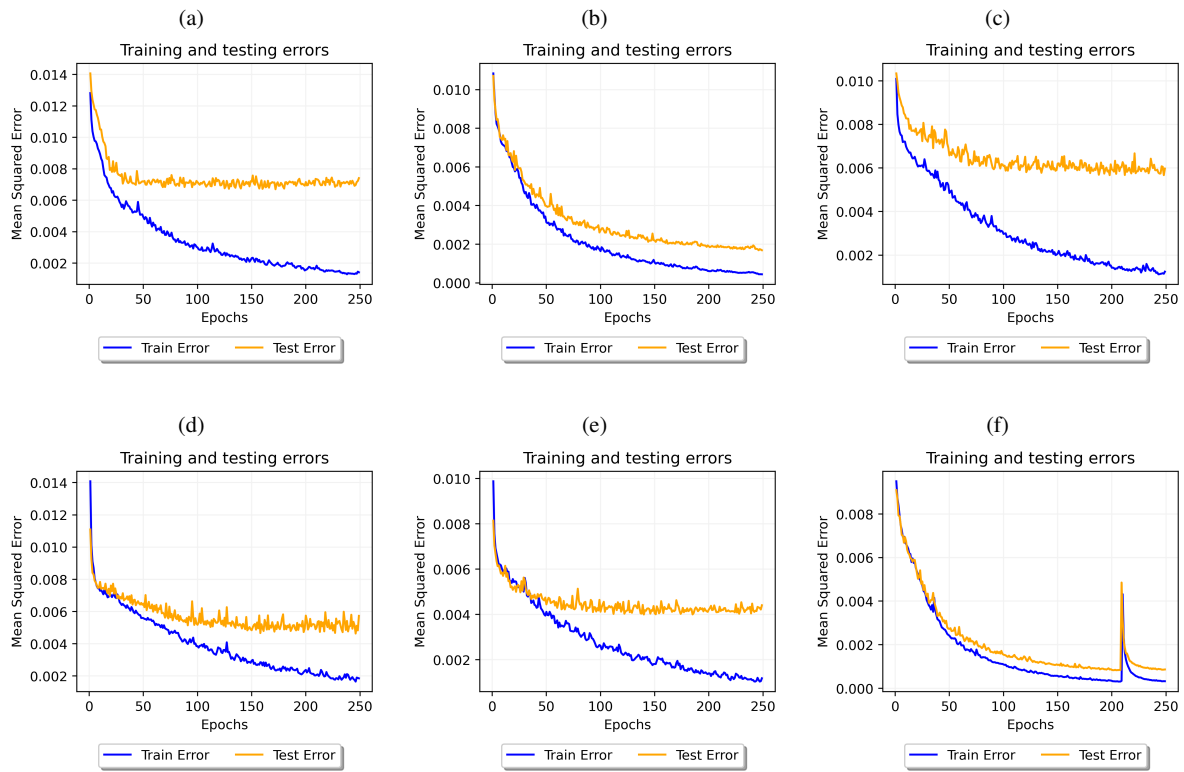


Figure 7: 7a: Prediction from baseline (pre-injection). 7b: Prediction from 1-2 hours post-injection. 7c: Prediction from 3-5 hours post-injection. 7d: Prediction from 5-7 hours post-injection. 7e: Prediction from 7-9 hours post-injection. 7f: Prediction from 1-9 hours post-injection.